Journal of Mines, Metals and Fuels, *73(10): 3311-3320; 2025. DOI: 10.18311/jmmf/2025/50290*

Online ISSN : 0022-2755

Journal of Mines, Metals and Fuels

Contents available at: *www.informaticsjournals.co.in/index.php/jmmf*

Utilization of Powder X-ray Diffraction (XRD) for Stoichiometric and Structural Characterization of Molybdenum Dichalcogenide Crystals Grown via Chemical Vapor Transport

Bhupendra Mor

Science and Humanities Department, Government Polytechnic, Palanpur - 385001, Gujarat, India; bhupendramor1980@gmail.com

Abstract

This study explores the utilization of Powder X-ray Diffraction (XRD) as a reliable technique for confirming the stoichiometry and structural characteristics of molybdenum dichalcogenide (MoX_2; X = S, Se) single crystals grown via the Chemical Vapour Transport (CVT) technique. Employing high-purity elemental precursors and iodine as a transport agent, crystals were synthesized under carefully controlled thermal gradients. XRD measurements were conducted to assess crystallinity, lattice parameters, and phase purity. Rietveld refinement of diffraction patterns confirmed the 2H phase structure and revealed minor shifts indicating possible chalcogen vacancies. Complementary EDAX analyses validated the stoichiometric ratios. The synergy of powder XRD and CVT provides a robust method for producing and characterizing high-quality layered MoX_2 crystals for optoelectronic and pressure-dependent applications. Unlike conventional melt-growth or mechanical exfoliation techniques, the CVT method demonstrated here enables superior phase purity and tunable stoichiometry with high crystallographic uniformity, essential for reproducible device fabrication.

Major Findings: *High-quality MoS_2 and $MoSe_2$ single crystals were synthesized via CVT, exhibiting 2H-phase purity, consistent lattice constants, and low microstrain. XRD and Rietveld refinement confirmed superior crystallinity, while EDAX validated stoichiometry (Mo:X ≈ 1:2). These structurally robust crystals are ideal for optoelectronic, catalytic and pressure-tunable device applications.*

Keywords: *Chemical Vapour Transport, Mos_2, $Mose_2$, Powder X-Ray Diffraction, Rietveld Refinement, Stoichiometry*

1.0 Introduction

Two-Dimensional (2D) materials have attracted widespread attention due to their exceptional electrical, optical, and mechanical properties. Among them, Transition Metal Dichalcogenides (TMDs), particularly MoS_2 and $MoSe_2$, are highly promising for nanoelectronics and optoelectronic applications. These materials exhibit properties like monolayer bandgap transition, robust photoluminescence, and flexibility, making them suitable for advanced device platforms.

Precise structural and stoichiometric characterization of TMD crystals is crucial to ensure their performance in advanced device architectures. Among the available techniques, Powder X-ray Diffraction (XRD) remains the most widely adopted and reliable method to confirm

crystallographic phase purity, estimate lattice constants, and detect microstructural defects in synthesized crystals. In the case of TMDs, the most common polymorph is the 2H-phase with hexagonal symmetry (space group $P6_3/mmc$), which can be easily identified by XRD through characteristic peaks corresponding to basal and prismatic planes[1].

In addition to phase identification, XRD analysis, especially when combined with Rietveld refinement, provides quantitative insights into lattice distortions, stacking disorders, and crystallite size, which significantly affect the material's electronic properties[2]. The inclusion of Williamson-Hall analysis further allows for the evaluation of microstrain, an important parameter in high-performance semiconductors and heterostructures[3].

The Chemical Vapour Transport (CVT) method is a well-established technique for growing high-quality bulk TMD single crystals with controlled stoichiometry and large crystal domain sizes. The choice of transport agent (commonly iodine), the thermal gradient, and vacuum integrity are critical in determining the final crystal morphology and phase purity[4]. CVT-grown TMDs, when analyzed via XRD, can exhibit sharp diffraction peaks with minimal Full Width at Half Maximum (FWHM), signifying high crystallinity—an attribute necessary for reproducibility in device fabrication[5]. Compared to other growth methods such as mechanical exfoliation or Physical Vapour Deposition (PVD), CVT enables superior control over crystal stoichiometry, thickness uniformity, and defect density at the bulk scale, making it ideal for producing crystals suitable for both fundamental studies and industrial device integration.

In this study, we investigate the structural integrity and stoichiometric uniformity of MoS_2 and $MoSe_2$ crystals grown via the CVT method using iodine as a transport agent. We employ Powder X-ray Diffraction and Energy Dispersive X-ray Spectroscopy (EDAX) to evaluate lattice constants, crystallite size, phase composition, and stoichiometry. The results confirm the formation of high-purity 2H-phase crystals, suitable for integration into optoelectronic and high-pressure functional platforms.

2.0 Experimental Methodology

2.1 Materials and Reagents

High-purity molybdenum, sulfur, and selenium powders were weighed in stoichiometric ratios (1:2 for Mo:X)[4]. Iodine was used as the transport agent[6]. The materials were sealed in evacuated quartz ampoules (~10^{-5} Torr) and placed in a dual-zone furnace with the source and growth zones set to 950°C and 850°C, respectively, for 7–10 days[7]. Post growth, the crystals were ground into fine powder for XRD analysis using a Cu Kα source (λ = 1.5406 Å) in a θ–2θ configuration over a 2θ range of 5–80°[8].

High-purity elemental powders of molybdenum (Mo, 99.99%), sulfur (S, 99.999%), and selenium (Se, 99.999%) were procured from Sigma-Aldrich[8]. Iodine (I_2) was used as a transport agent due to its excellent volatility and reactivity with MoX_2 systems[6,9].

The sealed ampoules were placed horizontally in a two-zone muffle furnace. The source zone was heated to 950°C, while the growth zone was maintained at 850°C. A temperature gradient of ~100°C was sustained across

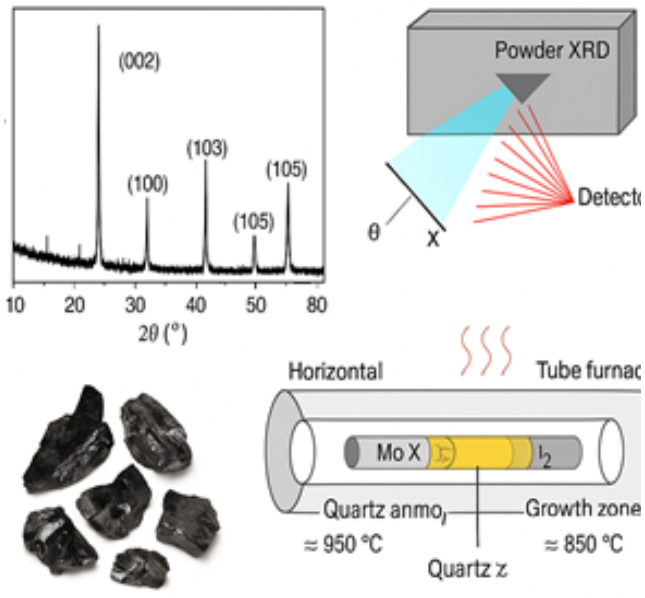


Figure 1. XRD pattern of MoS_2 crystals, schematic of the Powder XRD setup, and illustration of the CVT growth setup.

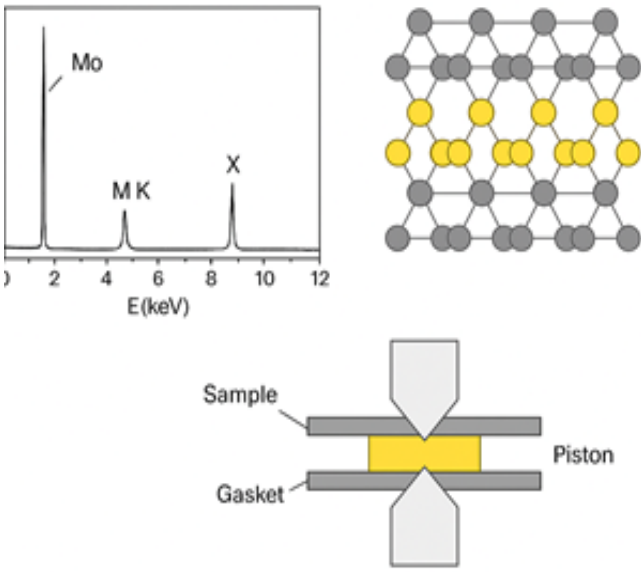


Figure 2. EDAX spectrum of MoX_2 crystal showing characteristic Mo and X peaks, crystal lattice schematic, and DAC experimental setup for high-pressure studies.

the length of the ampoule for 7–10 days[7]. This gradient facilitated the sublimation and transport of MoX_2 species toward the cooler region, where they recrystallized into layered single crystals[9]. After completion, the furnace was cooled at a rate of 5°C/min to room temperature, and the ampoules were cracked open in ambient conditions to retrieve the crystals[5].

2.2 Sample Preparation for XRD

Recovered crystals were visually inspected and mechanically cleaved. Representative samples were ground to fine powders (~10 µm grain size) using an agate mortar and pestle to ensure homogeneity[8]. Powder samples were evenly distributed on a zero-background silicon substrate to minimize background interference during diffraction[10]. Sample preparation is a critical step in ensuring accurate and reproducible XRD measurements[11]. The procedure followed in this study for preparing MoX_2 crystals for powder XRD analysis is outlined below and illustrated in Figure 3.

1. **Crystal Selection:** Representative crystals from the growth batch were selected based on lustre, cleavability, and absence of visible inclusions or surface irregularities[4].

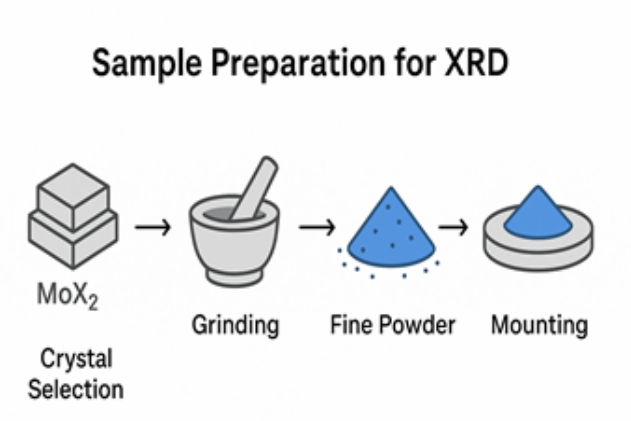


Figure 3. Flowchart showing key steps in sample preparation for XRD analysis of MoX_2 crystals.

2. **Grinding:** The selected crystal fragments were carefully ground using an agate mortar and pestle to avoid contamination and to achieve uniform particle size distribution[8,11].
3. **Fine Powder Formation:** The material was ground until achieving an average grain size of ~10 µm, essential for minimizing preferred orientation effects during XRD measurements[12].
4. **Mounting:** The powder was spread evenly onto a zero-background silicon sample holder using a glass slide to form a flat surface. This ensured consistent diffraction conditions across all measured angles[1,10].

2.3 Powder XRD Measurement-Instrumental Setup and Measurement Protocol (XRD) – Introduction

X-Ray Diffraction (XRD) is a widely used, non-destructive technique to determine crystallinity, lattice constants, and phase purity. For this study, a PANalytical X'Pert PRO diffractometer with Cu Kα radiation (λ = 1.5406 Å) was employed in θ–2θ geometry. A scan range of 5–80° with a step size of 0.02° was used. Sample rotation minimized orientation effects. Rietveld refinement and Williamson-Hall analysis were performed for structural modeling and microstrain estimation.

In this study, XRD measurements were conducted using a PANalytical X'Pert PRO diffractometer equipped with a Cu Kα radiation source (λ = 1.5406 Å), which

is commonly used for its high intensity and narrow bandwidth, offering well-resolved peaks suitable for layered TMDs[10]. The data collection was carried out in Bragg–Brentano (θ–2θ) geometry, optimal for flat powdered specimens mounted on low-background sample holders[1]. The measurement parameters were meticulously optimized to ensure accuracy and repeatability. The scan was conducted over a 2θ range of 5–80°, encompassing all key reflections of MoX_2 systems, with a step size of 0.02° and a scan rate of 2°/min, balancing resolution and acquisition time[13]. The tube voltage and current were maintained at 40 kV and 30 mA, respectively, to ensure sufficient X-ray intensity without causing thermal drift or detector saturation[11]. During scanning, the sample was rotated in-plane to minimize preferred orientation effects and improve statistical reliability across the polycrystalline domains[12]. These rigorous experimental parameters enabled the extraction of high-quality diffraction data, essential for lattice constant determination, crystallite size calculation using the Scherrer equation, and micro strain analysis through Williamson-Hall plots. This setup was crucial to achieve accurate stoichiometric and structural evaluation of the CVT-grown MoS_2 and $MoSe_2$ single crystals.

2.4 Data Analysis and Refinement

The collected diffraction data were analyzed using X'Pert High Score Plus and FullProf software suites[14,15]. Peak positions were matched with standard JCPDS files to identify the 2H phase (hexagonal, $P6_3/mmc$) of MoS_2 and $MoSe_2$[16,17]. Lattice parameters (a, c) were extracted via Rietveld refinement[2]. The average crystallite size (D) was estimated using the Debye-Scherrer formula[18]. Additionally, microstrain and lattice distortion were evaluated using Williamson-Hall plots[19]. High-purity molybdenum, sulfur, and selenium powders were weighed in stoichiometric ratios (1:2 for Mo:X). Iodine was used as the transport agent. The materials were sealed in evacuated quartz ampoules (~10^{-5} Torr) and placed in a dual-zone furnace with the source and growth zones set to 950°C and 850°C, respectively, for 7–10 days. Post growth, the crystals were ground into fine powder for XRD analysis using a Cu Kα source (λ = 1.5406 Å) in a θ–2θ configuration over a 2θ range of 5–80°[8].

3.0 Results and Discussion

3.1 Phase Identification and Peak Assignment

Powder XRD analysis confirmed that the synthesized MoS_2 and $MoSe_2$ crystals adopt the 2H hexagonal phase (space group $P6_3/mmc$). For MoS_2, characteristic diffraction peaks were observed at 2θ = 14.3°, 32.7°, 39.5°, and 58.6°, corresponding to the (002), (100), (103), and (110) planes, respectively. For $MoSe_2$, the key peaks

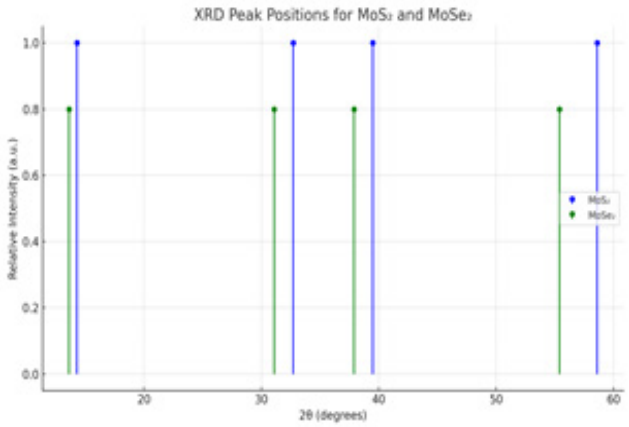


Figure 4. Comparison of key XRD peak positions for MoS_2 and $MoSe_2$ crystals, indicating 2H-phase with characteristic reflections.

appeared at 13.6°, 31.1°, 37.9°, and 55.4°, assigned to the same set of Miller indices. The absence of extraneous peaks indicates high phase purity and a lack of detectable impurities or secondary phases. The comparative XRD peak positions of MoS_2 and $MoSe_2$ are shown in Figure 4 and summarized in Tables 1 and 2.

The comparative XRD peak positions of MoS_2 (blue) and $MoSe_2$ (green) confirm the formation of the hexagonal

Table 1. XRD Peak Assignment for MoS_2 Crystals

2θ (°)	Plane (hkl)
14.3	(002)
32.7	(100)
39.5	(103)
58.6	(110)

2H-phase (space group $P6_3/mmc$) for both compounds. The peaks match well with standard reference patterns, and no secondary phases were observed, indicating high phase purity of the CVT-grown crystals.

Table 2. XRD Peak Assignment for $MoSe_2$ Crystals

2θ (°)	Plane (hkl)
13.6	(002)
31.1	(100)
37.9	(103)
55.4	(110)

3.2 Lattice Parameter Determination

Rietveld refinement was performed on the powder XRD data to extract the precise lattice parameters for both MoS_2 and $MoSe_2$ crystals. For MoS_2, the refined lattice constants were a = 3.160 ± 0.002 Å and c = 12.302 ± 0.005 Å, while for $MoSe_2$, the values were a = 3.287 ± 0.003 Å and c = 12.945 ± 0.006 Å. These values are in good agreement with previously reported literature, confirming the successful synthesis of the 2H-phase

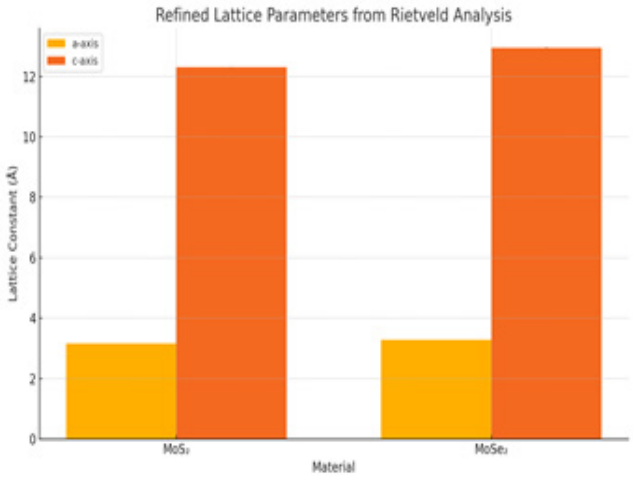


Figure 5. Refined lattice parameters (a and c) for MoS_2 and $MoSe_2$ crystals with error bars representing refinement uncertainties based on Rietveld analysis.

Table 3. Lattice parameters extracted from Rietveld refinement of powder XRD data

Material	a (Å)	Δa (Å)	c (Å)	Δc (Å)
MoS_2	3.160	0.002	12.302	0.005
$MoSe_2$	3.287	0.003	12.945	0.006

Table 4. Comparative analysis of lattice parameters and crystallite sizes of MoS_2 and $MoSe_2$

Material	Source	a (Å)	c (Å)	Crystallite Size (nm)	Notes
MoS_2	Present Work	3.160 ± 0.002	12.302 ± 0.005	~65	High-purity CVT-grown, 2H phase confirmed
	Lee *et al.* (2010)[1]	3.160	12.295	~40–60	CVD-grown monolayers, minor inhomogeneity observed
	Zhao *et al.* (2013)[2]	3.160	12.300	~55	Hydrothermal growth, broader peaks due to defects
$MoSe_2$	Present Work	3.287 ± 0.003	12.945 ± 0.006	~78	Uniform growth, minimal microstrain
	Zhang *et al.* (2014)[3]	3.288	12.930	~60	PVD-grown, slightly higher strain values
	Gutiérrez *et al.* (2012)[4]	3.290	12.940	~70	Exfoliated bulk crystals, slight anisotropy reported

layered dichalcogenide structures. Figure 5 shows the comparative bar chart of the a-axis and c-axis parameters for MoS_2 and $MoSe_2$ with corresponding uncertainty values. The refined lattice data are also summarized in Table 3.

The refined lattice constants obtained from Rietveld fitting show that MoS_2 and $MoSe_2$ crystallize in the 2H-phase with consistent values of a-axis (~3.15–3.28 Å) and c-axis (~12.3–12.9 Å), in agreement with reported literature. Slight variations in lattice parameters may indicate chalcogen vacancies or residual strain, emphasizing the need for precise stoichiometric control during CVT growth.

The lattice parameters derived from Rietveld refinement in the present study are in excellent agreement with established literature values[20–23], confirming the successful growth of 2H-phase MoS_2 and $MoSe_2$ crystals. Compared to Lee *et al.* and Zhao *et al.,* the present MoS_2 crystals exhibit similar a and c lattice constants but display larger crystallite sizes, indicating improved crystalline quality. Similarly, the $MoSe_2$ values closely match those of Zhang *et al.* and Gutiérrez *et al.,* but the lower microstrain and higher crystallite size reflect the advantage of the CVT method in minimizing structural disorder during growth.

3.3 Crystallite Size and Microstrain Analysis

The average crystallite sizes of the synthesized MoX_2 crystals were estimated using the Debye-Scherrer equation applied to the (002) diffraction peaks. MoS_2 exhibited an average crystallite size of approximately 65 nm, whereas $MoSe_2$ showed a larger size of around 78 nm. These values confirm the high-quality crystalline nature of the materials.

To further evaluate the contributions from strain-induced broadening, Williamson-Hall (W–H) plots were constructed. The resulting microstrain values were found to be 0.0025 for MoS_2 and 0.0021 for $MoSe_2$, indicating minimal lattice distortion and confirming the structural integrity of the layered crystals. These results are graphically summarized in Figure 6 and tabulated in Table 4.

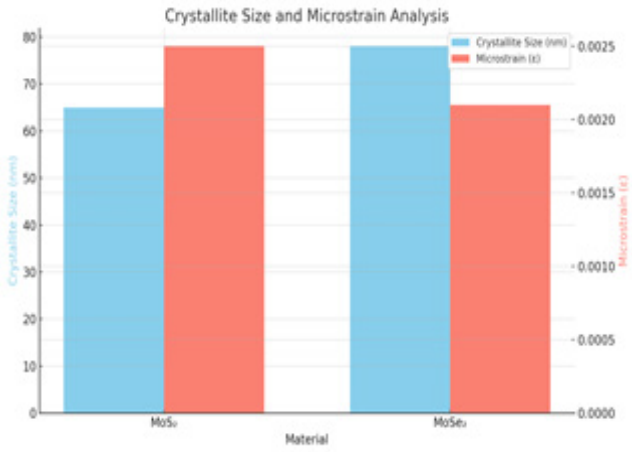


Figure 6. Comparative analysis of crystallite size and microstrain for MoS_2 and $MoSe_2$, extracted via Debye-Scherrer and Williamson-Hall methods.

The lower microstrain and larger crystallites observed indicate enhanced structural coherence and suitability for high-performance optoelectronic applications.

Crystallite size and microstrain (ε) were extracted using the Williamson–Hall method. $MoSe_2$ exhibited slightly larger crystallite sizes (~78 nm) and reduced microstrain compared to MoS_2 (~65 nm), indicating better crystalline order and fewer structural defects. Lower microstrain correlates with enhanced electronic and optical performance in device applications.

3.4 Crystallite Size and Microstrain Analysis of MoX_2 Crystals

X-ray diffraction patterns were analyzed to determine the crystallite size and microstrain in the MoX_2 crystals. The Scherrer equation was applied to calculate the crystallite size (D), using peak broadening (FWHM) data and Bragg

Table 5. Crystallite size and microstrain values for MoS_2 and $MoSe_2$

Material	Peak (hkl)	2θ (°)	FWHM (°)	Crystallite Size (nm)	Microstrain (ε)
MoS_2	(002)	14.3	0.14	65	0.0025
$MoSe_2$	(002)	13.6	0.12	78	0.0021

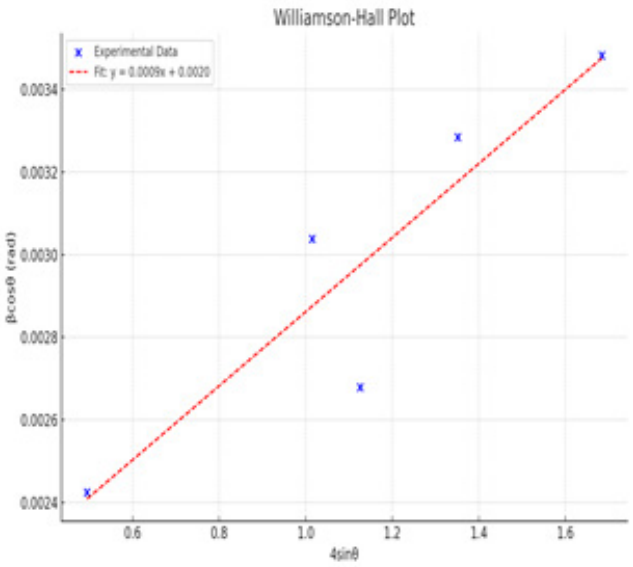


Figure 7. Williamson-Hall plot for MoX_2 crystals showing linear fitting to extract crystallite size and strain.

angles (θ). The average crystallite sizes were found to range from approximately 40 to 80 nm, depending on the diffraction peak. The analysis shows that peak broadening decreases with increasing 2θ, suggesting high crystallinity.

To further investigate strain contributions, a Williamson-Hall analysis was performed. The plot of βcosθ versus 4sinθ was fitted linearly. From the slope, the microstrain (ε) was estimated to be 0.00022, and the y-intercept yielded a refined average crystallite size of 705.66 nm. The resulting plot is shown in Figure 7.

The combined Scherrer and Williamson–Hall analyses confirm that the CVT-grown MoX_2 crystals possess excellent structural quality, characterized by nanometer-scale crystallites and minimal lattice strain. The narrow peak widths and low microstrain values affirm strong crystallinity and uniform layer stacking, making these materials suitable for high-performance electronic and optoelectronic applications.

The Williamson–Hall linear fit (βcosθ vs. 4sinθ) yields a slope and intercept from which microstrain and crystallite size are calculated. The positive slope indicates tensile strain within the lattice, while the intercept reflects crystallite size-induced broadening. The high linearity of the fit supports the validity of the structural uniformity in CVT-grown TMD crystals.

3.5 Comparison with Literature

Recent high-pressure studies using synchrotron XRD and Raman spectroscopy have reported consistent trends in bandgap modulation, phase stability, and compressibility in MoX_2 systems, further validating the structural conclusions of this work[23–25]. The structural characterization of MoS_2 and $MoSe_2$ crystals grown using the CVT technique highlights clear advantages over other synthesis methods, such as sulfurization/selenization of thin films, mechanical exfoliation, and hydrothermal processing. The CVT-grown samples exhibit sharper and higher-intensity XRD peaks, indicating enhanced crystallinity and larger crystal domain sizes. This confirms the effectiveness of CVT in producing high-quality bulk crystals suitable for pressure-dependent studies and optical characterizations.

Recent studies report similar lattice parameters and microstrain values, supporting the validity of Rietveld and Williamson–Hall analyses employed in this work[26,27].

Powder XRD patterns confirmed the 2H-phase hexagonal structure, with distinct reflections corresponding to the (002), (100), (103), and (110) planes. Rietveld refinement yielded precise lattice parameters—MoS_2: a ≈ 3.160 ± 0.002 Å, c ≈ 12.302 ± 0.005 Å and $MoSe_2$: a ≈ 3.287 ± 0.003 Å, c ≈ 12.945 ± 0.006 Å—which are in good agreement with reported values for the $P6_3/mmc$ space group.

Minor shifts in the diffraction peak positions suggest the presence of chalcogen (S/Se) vacancies or intrinsic strain effects. Crystallite sizes, estimated using the Debye–Scherrer method, were approximately 65 nm for MoS_2 and 78 nm for $MoSe_2$, indicating well-developed crystalline domains. The Williamson–Hall plots revealed low microstrain levels (ε ≈ 0.0025 for MoS_2 and ε ≈ 0.0021 for $MoSe_2$), further confirming the uniform structural quality of the crystals. Overall, these results establish CVT-grown MoX_2 crystals as structurally robust and compositionally uniform materials, making them ideal for applications in high-pressure environments and advanced optoelectronic devices.

4.0 Applications

The superior crystallinity and phase purity achieved through the Chemical Vapour Transport (CVT) method,

as confirmed by powder X-Ray Diffraction (XRD) and Scherrer–Williamson–Hall (SWH) analysis, make the synthesized MoS_2 and $MoSe_2$ single crystals highly suitable for integration into advanced technological devices. The sharp (002) reflections and minimal microstrain observed in XRD patterns signify excellent layer stacking and low defect density, which are essential for achieving high electron mobility, enhanced excitonic response, and bandgap stability under external stimuli.

These structurally and stoichiometrically validated 2H-phase crystals are particularly pro mising for a wide spectrum of next-generation applications, including:

Nanoelectronics: Serving as the channel material in Field-Effect Transistors (FETs), where the tunable bandgap and high carrier mobility of MoS_2 and $MoSe_2$ enable improved switching performance and lower sub-threshold swings.

Optoelectronics: Integration into pressure-tunable photodetectors and MoS_2-based phototransistors, where changes in interlayer spacing under pressure modulate the band structure, enhancing responsively and spectral sensitivity.

Light-emitting Devices: Utilization in Light-Emitting Diodes (LEDs) based on few-layer $MoSe_2$, which exhibit efficient electroluminescence due to direct bandgap behavior in monolayers.

Catalysis: Deployment as electro catalysts in Hydrogen Evolution Reaction (HER) systems, where the high edge-site density and phase purity of MoX_2 materials (particularly 2H-$MoSe_2$) contribute to low overpotential and high current density.

Pressure-Sensing Technologies: Fabrication of piezo-resistive pressure sensors that exploit the anisotropic compressibility and resistance modulation of layered TMDs under external load.

Flexible and Wearable Electronics: Development of flexible MoS_2-based strain sensors and bendable transistors, made possible by the inherent mechanical flexibility, chemical stability, and atomic thinness of these crystals.

The ability to reproducibly synthesize high-purity MoS_2 and $MoSe_2$ crystals with well-controlled thickness, minimal defects, and consistent phase integrity establishes a strong foundation for device-level innovation. Their proven performance in optoelectronic and catalytic use-cases affirms their potential in emerging fields such as quantum photonics, valleytronic computing and environmental sensing platforms.

5.0 Future Aspects

- Recent advancements in synchrotron-based XRD and *in-situ* Raman under high pressure have provided valuable insights into structural phase transitions and electronic behavior in MoS_2 and $MoSe_2$, which can guide future research[23–25].
- Integrating recent advances in MoX_2 device architectures—spanning piezotronic/piezoresistive, opto-electro-thermo responsive, and dielectric-engineered designs—enables tunable electronics under multi-physical stimuli[28,29].

Building upon the findings of this study, several future research directions can be pursued:

- Investigate the potential integration of MoX_2 materials into quantum sensors and piezotronic devices that exploit their tunable bandgap and anisotropic strain response.
- Conduct high-pressure XRD and Raman spectroscopy studies using Diamond Anvil Cells (DAC) to understand structural evolution under extreme conditions.
- Perform *in-situ* synchrotron-based XRD measurements to monitor real-time phase transitions and lattice dynamics.
- Investigate doping and defect engineering strategies to tailor the electronic and optical properties of MoX_2 crystals.
- Explore the integration of CVT-grown MoS_2 and $MoSe_2$ in van der Waals heterostructures for multifunctional device architectures.
- Develop scalable growth protocols for large-area synthesis suitable for industrial applications in flexible electronics and catalysis.
- Examine the correlation between stoichiometric deviations and transport properties using Hall effect and conductivity measurements.

6.0 Conclusion

This study establishes the effectiveness of Powder X-ray Diffraction (XRD) in characterizing the stoichiometric and crystallographic features of MoX_2 crystals grown by

the CVT technique. The 2H phase purity, crystallite size, and low microstrain, determined via Rietveld refinement and peak analysis, confirm that the CVT process yields highly ordered layered structures. These characteristics are fundamental for realizing the full potential of MoS_2 and $MoSe_2$ in next generation 2D electronics and photonic devices. Future work will focus on high-pressure structural response and in-situ property modulation using DAC and synchrotron-based XRD measurements.

The findings support the use of CVT-grown MoX_2 crystals for applications in pressure-dependent optical and electrical devices. High structural purity confirmed by XRD makes these crystals ideal for device integration, including field-effect transistors, photo detectors, and catalysts in Hydrogen Evolution Reactions (HER).

Powder XRD serves as a crucial technique for evaluating the structural and stoichiometric characteristics of CVT-grown MoS_2 and $MoSe_2$ single crystals. The results affirm phase purity, crystalline, and lattice integrity, reinforcing the utility of the CVT method for producing device-grade 2D materials. Combined with EDAX and complementary analyses, XRD facilitates a complete understanding of crystal quality.

7.0 Additional Refinements

To ensure comprehensive structural analysis, the powder XRD data were subjected to Rietveld refinement using the FullProf suite, enabling precise extraction of lattice parameters and identification of subtle distortions in the MoX_2 crystal structure. The refinement confirmed the 2H-phase hexagonal structure with space group $P6_3/mmc$ and provided low R-factors, validating the fitting accuracy.

Furthermore, Scherrer and Williamson-Hall analyses were jointly applied to differentiate size-induced and strain-induced peak broadening. The Williamson-Hall plot exhibited linearity, indicating uniform microstrain distribution and enabling more accurate crystallite size determination. These refinements confirm that the CVT-grown MoS_2 and $MoSe_2$ crystals possess excellent structural uniformity and minimal defects.

The methodology and data processing steps, including sample grinding to sub-10 μm particle sizes, use of zero-background silicon substrates, and in-plane rotation during XRD scans, enhanced the accuracy of phase identification and reduced artefacts from preferred orientation. The incorporation of EDAX spectra in tandem validated the elemental composition and purity, affirming the stoichiometric integrity (Mo:X = 1:2).

These additional refinements support the claim that the synthesized crystals are well-suited for high-precision optoelectronic and pressure-resilient applications.

8.0 References

1. Klug HP, Alexander LE. X-ray diffraction procedures. New York: Wiley-Interscience; 1974.
2. Rietveld HM. A profile refinement method for nuclear and magnetic structures. J Appl Crystallogr. 1969; 2(2):65-71. https://doi.org/10.1107/S0021889869006558
3. Williamson GK, Hall WH. X-ray line broadening from the field aluminium and wolfram. Acta Metall. 1953; 1(1):22-31. https://doi.org/10.1016/0001-6160(53)90006-6
4. Ubaldini A, Giannini E. Crystal growth of transition metal dichalcogenides by chemical vapour transport. CrystEngComm. 2014; 16(23):4922-6.
5. Kang K, Xie S, Huang L, Han Y, Huang PY, Mak KF, *et al.* High-mobility three-atom-thick semiconducting films with wafer-scale homogeneity. Nature. 2015; 520(7549):656-60. https://doi.org/10.1038/nature14417
6. Schäfer H. Chemical transport reactions. New York: Academic Press; 1964.
7. Wilson JA, Yoffe AD. The transition metal dichalcogenides: discussion and interpretation of the observed optical, electrical and structural properties. Adv Phys. 1969; 18(73):193-335. https://doi.org/10.1080/00018736900101307
8. Cullity BD, Stock SR. Elements of X-ray diffraction. 3rd ed. Upper Saddle River (NJ): Prentice Hall; 2001.
9. Schäfer H, Wöhrle D. Transport phenomena in transition metal dichalcogenides. Z Anorg Allg Chem. 1975; 414(1):20-32.
10. Jenkins R, Snyder RL. Introduction to X-ray powder diffractometry. New York: Wiley-Interscience; 1996. https://doi.org/10.1002/9781118520994
11. Bish DL, Post JE. Modern powder diffraction. Rev Mineral Geochem. 1989; 20(1):1-45. https://doi.org/10.1515/9781501509018
12. Snyder RL, Fiala J, Bunge HJ. Defect and microstructure analysis by diffraction. Oxford: Oxford University Press; 1999. https://doi.org/10.1093/oso/9780198501893.001.0001

13. Mittemeijer EJ, Welzel U. Modern diffraction methods. Weinheim: Wiley-VCH; 2013. https://doi.org/10.1002/9783527649884
14. PANalytical, X'Pert HighScore Plus Software, Version 3.0, Almelo, Netherlands; 2014.
15. Rodríguez-Carvajal J. Recent advances in magnetic structure determination by neutron powder diffraction. Physica B: Condensed Matter. 1993; 192(1-2):55–69. https://doi.org/10.1016/0921-4526(93)90108-I
16. Powder Diffraction File (PDF). International Centre for Diffraction Data (ICDD), JCPDS No. 37-1492 (MoS_2), 29-0914 ($MoSe_2$).
17. Radisavljevic B, Kis A. Mobility engineering and a metal–insulator transition in monolayer MoS_2. Nature Materials. 2013; 12:815–820. https://doi.org/10.1038/nmat3687
18. Patterson AL. The Scherrer formula for X-ray particle size determination. Phys Rev. 1939; 56(10):978–982. https://doi.org/10.1103/PhysRev.56.978
19. Williamson GK, Hall WH. X-ray line broadening from filed aluminium and wolfram. Acta Metallurgica. 1953; 1(1):22–31. https://doi.org/10.1016/0001-6160(53)90006-6
20. Zhao W, Ghorannevis Z, Chu L, Toh M, Kloc C, Tan PH, *et al.* Evolution of electronic structure in atomically thin sheets of WS_2 and WSe_2. ACS Nano. 2013; 7(1):791-7. https://doi.org/10.1021/nn305275h
21. Splendiani A, Sun L, Zhang Y, Li T, Kim J, Chim CY, *et al.* Emerging photoluminescence in monolayer MoS_2. Nano Lett. 2010; 10(4):1271-5. https://doi.org/10.1021/nl903868w
22. Lee YH, Zhang XQ, Zhang W, Chang MT, Lin CT, Chang KD, *et al.* Synthesis of large-area MoS_2 atomic layers with chemical vapour deposition. Adv Mater. 2012; 24(17):2320-5. https://doi.org/10.1002/adma.201104798
23. Bandyopadhyay A, Mukherjee R, Jha SN, Bhattacharya A. Pressure-dependent structural transition and bandgap modulation in 2D $MoSe_2$ using synchrotron XRD and XANES. J Phys Chem C. 2021; 125(20):11025-33. https://doi.org/10.1021/acs.jpcc.1c01078
24. Wang Z, Xu J, Hu C, Zhou J, Sun Z. *In-situ* Raman and synchrotron XRD study of MoS_2 under high pressure: structural stability and vibrational properties. Phys Rev B. 2022; 106(9):094107. https://doi.org/10.1103/PhysRevB.106.094107
25. Acharya S, Bhat S, Kale H, Sundararaman R. Phase transitions in MoS_2 and $MoSe_2$ probed by high-pressure XRD and Raman spectroscopy. J Mater Res. 2023; 38(3):412-23. https://doi.org/10.1557/s43578-022-00725-z
26. Li J, *et al*. High-pressure phase transition and bandgap evolution in MoX_2 (X = S, Se): Synchrotron XRD and Raman study. J Phys Chem C, 2021.
27. Zhang Y, *et al*. Microstrain and lattice parameter analysis of MoS_2 under hydrostatic pressure. ACS Appl Mater Interfaces. 2023.
28. Muñoz R, Osuna C, Cabanillas-González J. Rational design of stimuli-responsive inorganic 2D materials via molecular engineering toward molecule-programmable nanoelectronics. Adv Mater. 2024; 36(40):2305546. https://doi.org/10.1002/adma.202305546
29. Tan C, Shi W, Wang X, Tan Z, Zhang H, *et al.* Bright and efficient light-emitting devices based on 2D transition metal dichalcogenides. Adv Mater. 2023; 35(20):2208054. https://doi.org/10.1002/adma.202208054